

Periodically driven model with quasiperiodic potential and staggered hopping amplitudes: engineering of mobility gaps and multifractal states

Sreemayee Aditya¹, K. Sengupta² and Diptiman Sen¹

¹Centre for High Energy Physics, Indian Institute of Science, Bengaluru 560012, India

²School of Physical Sciences, Indian Association for the Cultivation of Science, Jadavpur, Kolkata 700032, India

We study the effects of periodic driving of a one-dimensional model with a quasiperiodic potential V_0 and nearest-neighbor hopping amplitudes which have a uniform term which varies periodically in time with frequency ω and a staggered term which is time-independent. We find numerically that there are multiple mobility gaps in the Floquet spectrum of such a model that separate different bands of quasienergies. We also find that there are ranges of ω and V_0 where there are multifractal states whose generalized inverse participation ratios scale with the system size with exponents which are different from the values for both extended and localized states. We see re-entrant transitions between the different kinds of states when ω and V_0 are varied. The presence of such states is also confirmed by the behavior of the Shannon entropy. Many of our numerical results can be understood from an analytic Floquet Hamiltonian derived using a Floquet perturbation theory that uses the inverse of the driving amplitude as the perturbation parameter. In the limit of high frequency and large driving amplitude, we find that the Floquet quasienergies match the energies of the undriven system, but the Floquet eigenstates are much more extended. We also study the spreading of a one-particle wave packet and find that it is always ballistic but the ballistic velocity varies significantly with the system parameters, sometimes showing a non-monotonic dependence on V_0 . Finally, we compare the results for the model with staggered hopping amplitudes with a model with uniform hopping amplitudes, and we find some significant differences between the two cases.

I. INTRODUCTION

Periodically driven systems have been studied extensively for the last several years because of the multitude of unusual phenomena that they can exhibit^{1–8}. For instance, periodic driving can be used to engineer topological states of matter^{9–14}, Floquet time crystals^{15–17} and other novel steady states^{18,19}, produce dynamical localization^{20–23}, dynamical freezing^{24–26} and other dynamical transitions^{27–37}, tune a system into ergodic or non-ergodic phases^{38–40}, and generate emergent conservation laws⁴¹.

The effects of periodic driving on localization-delocalization transitions have been relatively less studied^{42,43}. A well-studied *time-independent* model in one dimension model with a localization-delocalization transition is the Aubry-André model^{44,45}. This is a tight-binding model with uniform nearest-neighbor hopping amplitude γ and a quasiperiodic on-site potential with strength V_0 . Depending on the value of V_0 , this model is known to have two phases, with all states being extended (localized) for V_0 smaller (larger) than some critical value; the critical value of V_0 is known to be equal to 2γ . Studies of other variants of this system have shown that multiple localization transitions and states with multifractal properties can appear^{46,47}. Given these different possibilities for an undriven system, it would be interesting to study what can happen if a system with both a quasiperiodic potential and a staggered hopping amplitude is driven periodically in time. In particular, we would like to understand if the driving can generate mobility edges or gaps, and whether states which are neither extended nor localized can appear⁴⁸. (See Ref. 49 for a recent experiment on a kicked system with a quasiperiodic potential).

The plan of this paper is as follows. In Sec. II we present the Hamiltonian of our model consisting of a staggered time-independent hopping with values γ_1 and γ_2 on alternating

sites, and a uniform time-periodic hopping with amplitude a (both hopping amplitudes are between nearest neighbors only), and a quasiperiodic on-site potential with strength V_0 . In the limit where both the driving amplitude and the frequency are much larger than the time-independent hopping amplitudes and V_0 (i.e., $a, \omega \gg \gamma_1, \gamma_2, V_0$), we use a Floquet perturbation theory to first order in order to analytically derive an effective time-independent Hamiltonian H_F called the Floquet Hamiltonian. Both sinusoidal driving and driving by a periodic square pulse are considered. In Sec. III we numerically study the properties of the eigenstates of the Floquet operator U (in particular, their scaling with the system size L to see if they are localized, extended or multifractal), and whether there are any mobility edges or gaps. We compare the results obtained numerically from the Floquet operator with those obtained from the Floquet Hamiltonian. We also study the Shannon entropy, the spreading of a wave packet and the structure of the Floquet Hamiltonian in real space to shed more light on the degree of localization of the Floquet eigenstates. The form of the Floquet eigenstates and eigenvalues in the high-frequency limit is studied. In Sec. IV we consider the case where the time-independent hopping amplitudes are uniform ($\gamma_1 = \gamma_2$) in order to contrast with the case of staggered hopping amplitudes. In Sec. V we summarize our results and point out some directions for future studies.

Our main results are as follows. We find that at intermediate driving frequencies ω and large values of the quasiperiodic potential strength V_0 , there are eigenstates of the Floquet operator which are neither extended nor localized. The scaling with the system size of the generalized inverse participation ratio of these states indicates a multifractal nature, and this is qualitatively confirmed by the average Shannon entropy of these states. This is true for both sinusoidal driving and square pulse driving. In the high-frequency limit, we find that the spectrum of Floquet quasienergies approaches the energy

spectrum of the model with no driving. However, when the driving amplitude is also large, we find that the Floquet eigenstates are significantly different from those of the undriven system; typically, driving makes the states much more extended. We find that one-particle wave packets always spread ballistically though the ballistic velocity varies considerably depending on the system parameters. In conclusion, we show that a combination of quasiperiodic potential, periodic driving of the uniform hopping amplitude and a time-independent staggered hopping hopping gives rise to a wide range of unusual properties of the Floquet eigenstates.

II. MODEL HAMILTONIAN AND FLOQUET PERTURBATION THEORY

In this section, we will study a one-dimensional model with both uniform and staggered nearest-neighbor hopping amplitudes and a quasiperiodic on-site potential. We will first consider what happens when the uniform hopping amplitude is driven sinusoidally in time with a frequency ω and an amplitude a . Later we will study what happens when the driving is given by a periodic square pulse. The Hamiltonian of the system is given by

$$H(t) = \sum_j [(a \sin(\omega t) + \gamma_1) (a_j^\dagger b_j + b_j^\dagger a_j) + (a \sin(\omega t) + \gamma_2) (a_j^\dagger b_{j-1} + b_{j-1}^\dagger a_j) + V_0 \{\cos(2\pi\beta(2j-1)) a_j^\dagger a_j + \cos(2\pi\beta(2j)) b_j^\dagger b_j\}], \quad (1)$$

where the quasiperiodic potential has strength V_0 , and we take $\beta = (\sqrt{5} - 1)/2$ so that it is irrational. We have taken the unit cells, labeled by an integer j , to consist of two sites labeled as a_j and b_j . We will set the nearest-neighbor spacing to be equal to 1; hence the size of a unit cell is 2. We will impose periodic boundary conditions and take the system to have a total of L sites. (As we will discuss later, for our numerical calculations we will allow β to deviate in a minimal way from $(\sqrt{5} - 1)/2$ in order to have periodic boundary conditions). Note that we have allowed the time-independent hopping amplitudes to be different on alternate bonds (γ_1 and γ_2), but we take the driving term to be the same on all bonds. In this paper, we will mainly study the limit of the staggered hopping model in which $\gamma_2 = -\gamma_1$. We will also study the case of uniform hopping with $\gamma_2 = \gamma_1$ and compare the results found there with those obtained for $\gamma_2 = -\gamma_1$. We note that in the absence of driving ($a = 0$), the model reduces to the Aubry-André model. Further, the model with $\gamma_2 = -\gamma_1$ can be mapped by a unitary transformation ($a_j \rightarrow -a_j$ and $b_j \rightarrow b_j$) to a model with uniform hopping amplitudes ($\gamma_2 = \gamma_1$), but this transformation cannot be done if the driving term is present ($a \neq 0$). We will set $\hbar = 1$ in this paper.

We now compute the Floquet Hamiltonian using first-order Floquet perturbation theory (FPT) for a , $\omega \gg \gamma_1, \gamma_2, V_0$.^{8,38,41,50} FPT is a method for deriving the Floquet Hamiltonian in the limit where the driving amplitude is much

larger than the coefficients of the time-independent terms in the Hamiltonian. In that limit, FPT is more powerful than the Magnus expansion which is often used in the high-frequency limit^{4,6}; unlike the Magnus expansion, FPT does not involve expanding in powers of $1/\omega$. To develop FPT for our model, we write the Hamiltonian as $H(t) = H_0(t) + V_1 + V_2$, where, in terms of a momentum k (which lies in the range $[-\pi/2, \pi/2]$),

$$H_0(t) = \sum_k [a \sin(\omega t) (1 + e^{-2ik}) a_k^\dagger b_k + \text{H.c.}], \quad (2)$$

and the perturbation has two parts,

$$\begin{aligned} V_1 &= \sum_k [(\gamma_1 + \gamma_2 e^{-2ik}) a_k^\dagger b_k + \text{H.c.}], \\ V_2 &= \sum_{k,k'} [f_1(k, k') a_k^\dagger a_{k'} + f_2(k, k') b_k^\dagger b_{k'}], \end{aligned} \quad (3)$$

with

$$\begin{aligned} f_1(k, k') &= \frac{2V_0}{L} \sum_j \cos[4\pi\beta(j - \frac{1}{2})] e^{-2i(k-k')j}, \\ f_2(k, k') &= \frac{2V_0}{L} \sum_j \cos[4\pi\beta j] e^{-2i(k-k')j}. \end{aligned} \quad (4)$$

We note that the Fourier transform of the quasiperiodic potential couples different momenta which is a consequence of the fact that such a potential breaks translation symmetry. More specifically, $f_1(k, k')$ and $f_2(k, k')$ are non-zero whenever $k - k' = \pm 2\pi\beta \bmod \pi$.

The instantaneous eigenvalues of $H_0(t)$ are given by

$$E_{k\pm} = \pm 2a \sin(\omega t) \cos(k). \quad (5)$$

These satisfy the condition

$$e^{i \int_0^T dt [E_{k+}(t) - E_{k-}(t)]} = 1, \quad (6)$$

where $T = 2\pi/\omega$ is the time period of the drive. We therefore have to carry out degenerate FPT. The eigenfunctions corresponding to $E_{k\pm}$ are given by

$$|k\pm\rangle = \frac{1}{\sqrt{2}} \begin{pmatrix} 1 \\ \pm e^{ik} \end{pmatrix}, \quad (7)$$

We begin with the Schrödinger equation

$$i \frac{d|\psi\rangle}{dt} = (H_0 + V) |\psi\rangle, \quad (8)$$

where $V = V_1 + V_2$. We assume that $|\psi(t)\rangle$ has the expansion

$$|\psi(t)\rangle = \sum_n c_n(t) e^{-i \int_0^t dt' E_n(t')} |n\rangle. \quad (9)$$

Eq. (8) then implies that

$$\frac{dc_m}{dt} = -i \sum_n \langle m|V|n\rangle e^{i \int_0^t dt' (E_m(t') - E_n(t'))} c_n. \quad (10)$$

Integrating this equation, and keeping terms only to first order in V , we find that

$$c_m(T) = c_m(0) - i \sum_n \int_0^T dt \langle m|V|n\rangle \times e^{i \int_0^t (E_m(t') - E_n(t')) dt'} c_n(0). \quad (11)$$

This can be written as

$$c_m(T) = \sum_n \left(I - i H_F^{(1)} T \right)_{mn} c_n(0), \quad (12)$$

where I denotes the identity matrix and $H_F^{(1)}$ is the Floquet Hamiltonian to first order in V .

The calculation proceeds as follows. First, we consider $H_{F1}^{(1)} = \sum_k H_{Fk1}^{(1)}$ which is proportional to V_1 . This term has non-zero matrix elements between states with the same momenta, and it yields

$$\begin{aligned} \langle k \pm | H_{Fk1}^{(1)} | k \pm \rangle &= \pm (\gamma_1 + \gamma_2) \cos(k), \\ \langle k + | H_{Fk1}^{(1)} | k - \rangle &= -i (\gamma_1 - \gamma_2) \sin(k) J_0(\mu_k) e^{i\mu_k}, \\ \mu_k &= \frac{4a \cos(k)}{\omega}. \end{aligned} \quad (13)$$

Using Eq. (13), we write $H_{Fk1}^{(1)}$ as

$$\begin{aligned} H_{Fk1}^{(1)} &= (\gamma_1 + \gamma_2) \cos(k) \sigma_z \\ &+ (\gamma_1 - \gamma_2) J_0(\mu_k) \cos(\mu_k) \sin(k) \sigma_y \\ &+ (\gamma_1 - \gamma_2) J_0(\mu_k) \sin(\mu_k) \sin(k) \sigma_x. \end{aligned} \quad (14)$$

where we have defined the Pauli matrices $\sigma_{x,y,z}$ in the $|k+\rangle$, $|k-\rangle$ basis.

Next, we change basis to

$$|k \uparrow\rangle = a_k^\dagger |0\rangle, \quad |k \downarrow\rangle = b_k^\dagger |0\rangle, \quad (15)$$

so that

$$|k \pm\rangle = \frac{1}{\sqrt{2}} (|k \uparrow\rangle \pm e^{ik} |k \downarrow\rangle). \quad (16)$$

Using a two-component operator $\psi_k = (a_k, b_k)$, we can write $H_{F1}^{(1)}$ in the new basis as

$$\begin{aligned} H_{F1}^{(1)} &= \frac{1}{2} \sum_k \psi_k^\dagger \begin{pmatrix} \alpha_{2k} & \alpha_{1k} \\ \alpha_{1k}^* & -\alpha_{2k} \end{pmatrix} \psi_k \\ \alpha_{1k} &= g_{1k} [1 + J_0(\mu_k) \cos(\mu_k)] \\ &+ g_{2k} [1 - J_0(\mu_k) \cos(\mu_k)], \\ g_{1k} &= \gamma_1 + \gamma_2 e^{-2ik}, \quad g_{2k} = \gamma_2 + \gamma_1 e^{-2ik}, \\ \alpha_{2k} &= (\gamma_1 - \gamma_2) \sin(k) J_0(\mu_k) \sin(\mu_k). \end{aligned} \quad (17)$$

We note that if $\gamma_2 = \gamma_1$, we obtain $\alpha_{1k} = 2\gamma_1(1 + e^{-i2k})$ and $\alpha_{2k} = 0$. Hence $H_{F1}^{(1)}$ does not depend on the driving parameters ω and a . It is possible that higher order terms will depend on the driving parameters when $\gamma_2 = \gamma_1$ but these terms will be smaller than the first-order term derived here. We therefore expect that driving will have a smaller effect when $\gamma_2 = \gamma_1$ compared to $\gamma_2 = -\gamma_1$.

Next, we compute the first-order contribution to the Floquet Hamiltonian, $H_{F2}^{(1)}$, arising from V_2 . To this end, we first define

$$\begin{aligned} p_\pm(k, k') &= \frac{1}{2} (f_1(k, k') \pm f_2(k, k') e^{-i(k-k')}), \\ q_\pm(k, k') &= \frac{1}{2} (f_2(k, k') \pm f_1(k, k') e^{i(k-k')}), \\ r_\pm(k, k') &= \frac{i}{2} (f_2(k, k') e^{-ik} \pm f_1(k, k') e^{-ik'}), \\ t_\pm(k, k') &= \frac{i}{2} (f_1(k, k') e^{ik} \pm f_2(k, k') e^{ik'}), \\ \mu_{kk'}^\pm &= \frac{1}{2} (\mu_k \pm \mu_{k'}). \end{aligned} \quad (18)$$

We then find that in the $|k\pm\rangle$ basis, the matrix elements of $H_{F2}^{(1)}$ are given by

$$\langle ks | H_{F2}^{(1)} | k's' \rangle = p_{ss'}(k, k') J_0(\mu_{kk'}^{-ss'}) e^{is\mu_{kk'}^{-ss'}}, \quad (19)$$

where $ss' = +1$ if $s = s' = +1$ or $s = s' = -1$, and $ss' = -1$ if $s = +1$, $s' = -1$ or $s = -1$, $s' = +1$.

Using Eq. (16), we find that H_{F2} is diagonal in the $|k \uparrow\rangle$, $|k \downarrow\rangle$ basis and takes the form

$$\begin{aligned} H_{F2}^{(1)} &= [\cos(\mu_{kk'}^-) J_0(\mu_{kk'}^-) p_+(k, k') + \cos(\mu_{kk'}^+) J_0(\mu_{kk'}^+) p_-(k, k')] a_k^\dagger a_{k'} \\ &+ [\cos(\mu_{kk'}^-) J_0(\mu_{kk'}^-) q_+(k, k') + \cos(\mu_{kk'}^+) J_0(\mu_{kk'}^+) q_-(k, k')] b_k^\dagger b_{k'} \\ &+ [\sin(\mu_{kk'}^-) J_0(\mu_{kk'}^-) r_+(k, k') + \sin(\mu_{kk'}^+) J_0(\mu_{kk'}^+) r_-(k, k')] a_k^\dagger b_{k'} \\ &+ [\sin(\mu_{kk'}^-) J_0(\mu_{kk'}^-) t_+(k, k') + \sin(\mu_{kk'}^+) J_0(\mu_{kk'}^+) t_-(k, k')] b_k^\dagger a_{k'}. \end{aligned} \quad (20)$$

This completes our derivation of the first-order Floquet Hamiltonian within FPT.

We can follow the same procedure to find the Floquet Hamiltonian for square pulse driving. We consider a driving protocol having the form

$$\begin{aligned} f(t) &= a \text{ for } 0 \leq t \leq T/2, \\ &= -a \text{ for } T/2 \leq t \leq T. \end{aligned} \quad (21)$$

The form of the first-order Floquet Hamiltonian for square pulse driving is similar to the form we obtained for sinusoidal driving except that $J_0(x)$ has to be replaced by $\sin(x)/x$ and $\mu_k = 4a \cos(k)/\omega$ has to be replaced by $\mu_k = aT \cos(k)$. A square pulse driving is easier to study numerically since the Floquet operator U which time-evolves the system for one time period T can be obtained by simply multiplying two operators, one which time-evolves from $t = 0$ to $T/2$ and the other which evolves from $t = T/2$ to T .

We now look at the form of $H_F^{(1)}$ in the limits $\omega \gg a \gg \gamma_1, \gamma_2, V_0$ and $a \gg \omega \gg \gamma_1, \gamma_2, V_0$, which we will refer to as the high- and intermediate-frequency regimes respectively. In both cases, we are assuming that $\omega \gg \gamma_1, \gamma_2, V_0$. If this condition is not satisfied (i.e., if we are in the low-frequency regime), the Floquet Hamiltonian H_F cannot be uniquely defined since the eigenvalues $e^{-i\theta_m}$ of the Floquet operator U will not satisfy $|\theta_m| \ll \pi$ for all the Floquet eigenstates m . Hence $H_F = (i/T) \ln U$ will suffer from branch cut ambiguities. This necessitates folding back of Floquet eigenstates into the first Floquet Brillouin zone⁴⁰, a technical complication which we will avoid in this work.

We first consider the case of sinusoidal driving and look at the two limits separately.

(i) The high-frequency limit can be studied using either the FPT described above or the Magnus expansion. In the FPT, we have $\mu_k = (4a/\omega) \cos(k) \rightarrow 0$ for all k lying in the range $[-\pi/2, \pi/2]$. Since the Bessel function satisfies $J_0(z) \rightarrow 1$ when $z \rightarrow 0$, we find that $H_{F1}^{(1)} + H_{F2}^{(2)}$ approaches the time-independent part, $V_1 + V_2$, of the Hamiltonian $H(t)$ given in Eq. (3). Hence, the high-frequency limit should give the same results as the undriven system with $a = 0$. However, we will see later that although this is true for the Floquet eigenvalues, it does not seem to hold for the Floquet eigenstates.

(ii) The intermediate-frequency limit cannot be studied using the Magnus expansion, and we have to use the FPT. We now use the fact that $J_0(z)$ goes to zero as $\sqrt{2/(\pi z)} \cos(z - \pi/4)$ when $|z| \rightarrow \infty$. Further, $\mu_k \rightarrow \pm\infty$ except near the special point $k = \pi/2$. Similarly, $\mu_{kk'}^\pm = (1/2)(\mu_k \pm \mu_{k'}) \rightarrow \pm\infty$ except near the point $(k, k') = (\pi/2, \pi/2)$ and the line $k = \pm k'$. However, we saw after Eq. (4) that the functions $f_1(k, k')$ and $f_2(k, k')$ are non-zero only if $k - k' = \pm 2\pi\beta \bmod \pi$. Since $\beta = (\sqrt{5} - 1)/2 \simeq 0.618$, and k, k' lie in the range $[-\pi/2, \pi/2]$, we take $2\pi\beta \bmod \pi$ to be equal to either $(\sqrt{5} - 2)\pi \simeq 0.742$ or $(\sqrt{5} - 3)\pi \simeq -2.400$, so that $k - k' \simeq 0.742$ or -2.400 . Putting together the conditions arising from $\mu_{kk'}^\pm$, $f_1(k, k')$ and $f_2(k, k')$, we see that in Eq. (20), the terms involving products of $J_0(\mu_{kk'}^\pm)$ and $f_1(k, k')$ or $f_2(k, k')$ will go to zero at all values of k, k'

except near the four points $(k, k') \simeq \pm(0.742/2)(1, -1)$ or $\pm(2.400/2)(1, -1)$. Ignoring these special points, we see that in the intermediate-frequency limit, $H_{F2}^{(1)} \rightarrow 0$ in Eq. (20), which implies that the effect of the quasiperiodic potential goes to zero. Similarly, we see that except near the special point $k = \pi/2$, $J_0(\mu_k) \rightarrow 0$, and $H_{F1}^{(1)}$ in Eq. (17) approaches the form

$$H_{F1}^{(1)} = \frac{1}{2}(\gamma_1 + \gamma_2) \sum_k \psi_k^\dagger \begin{pmatrix} 0 & 1 + e^{-i2k} \\ 1 + e^{i2k} & 0 \end{pmatrix} \psi_k. \quad (22)$$

This describes a system with uniform hopping amplitude $(1/2)(\gamma_1 + \gamma_2)$ on all bonds. We thus see that in the intermediate-frequency limit, the system approaches a simple limit in which the hopping amplitude is uniform and there is no quasiperiodic potential. The quasienergies will then be given by $(\gamma_1 + \gamma_2) \cos(k)$ which is a gapless spectrum.

We reach similar conclusions in the case of square pulse driving. Namely, the high-frequency limit is the same as an undriven system with staggered hopping amplitudes γ_1, γ_2 and a quasiperiodic potential V_0 , while the intermediate-frequency limit is a system with a uniform hopping amplitude $(1/2)(\gamma_1 + \gamma_2)$ and no quasiperiodic potential.

Finally, we discuss some exact symmetries of the Floquet Hamiltonian. We can show that the Floquet Hamiltonian for the present problem can only have terms proportional to odd powers of V_1 and V_2 for a drive satisfying the condition $f(-t) = -f(t)$ (which is satisfied if $f(t)$ is either given by $a \sin(\omega t)$ or by the square pulse form in Eq. 21). To see this, we first show that the Floquet operator U satisfies

$$U^{-1}(a, \gamma_1, \gamma_2, V_0) = U(a, -\gamma_1, -\gamma_2, -V_0). \quad (23)$$

Hence the Floquet Hamiltonian H_F , which satisfies $U = e^{-iH_F T}$, must satisfy

$$H_F(a, \gamma_1, \gamma_2, V_0) = -H_F(a, -\gamma_1, -\gamma_2, -V_0). \quad (24)$$

Hence H_F can only have odd powers of γ_1, γ_2 and V_0 . As a result, the next correction after the terms of first-order in γ_1, γ_2 and V_0 will be of third order and will therefore be small. Hence, in the following sections we will only show the perturbative results based on first-order FPT.

III. RESULTS FOR THE MODEL WITH $\gamma_2 = -\gamma_1$

The Floquet Hamiltonian obtained in Sec. II allows us to study the properties of the Floquet eigenstates within first-order FPT. To this end, we numerically diagonalize $H_F^{(1)} = H_{F1}^{(1)} + H_{F2}^{(1)}$ to obtain its eigenvectors and eigenvalues

$$H_F^{(1)} |\psi_m^{(1)}\rangle = E_{Fm}^{(1)} |\psi_m^{(1)}\rangle. \quad (25)$$

On the other hand, the Floquet operator U will have eigenvectors $|\psi_m\rangle$ and corresponding eigenvalues $\exp(-i\theta_m)$, where $\theta_m = E_{Fm}T$ can be chosen to lie in the range $[-\pi, \pi]$. Then the quasienergies E_{Fm} obtained from θ_m will lie in the range

$[-\omega/2, \omega/2]$.

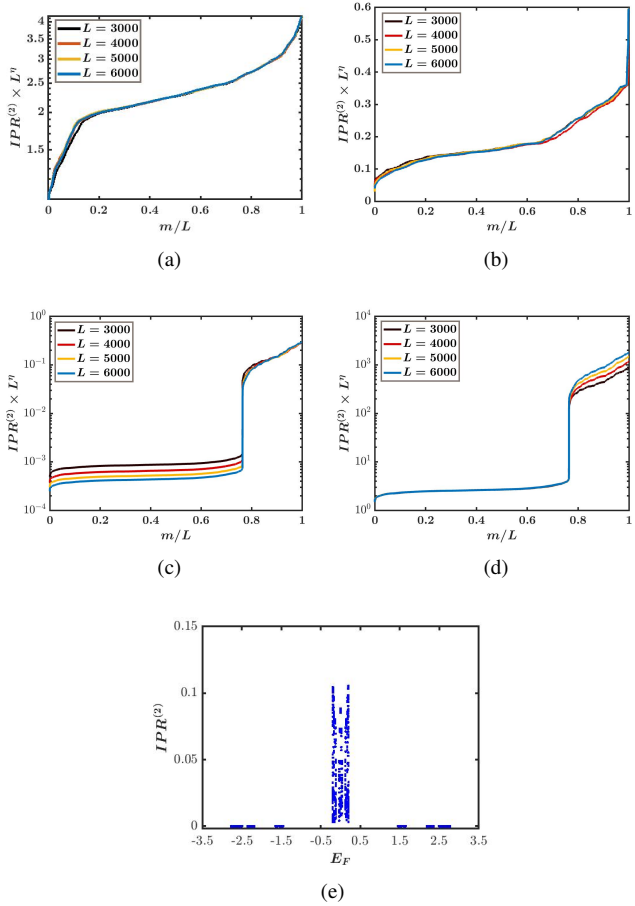


FIG. 1: (a-d) Plots of $I_m^{(2)} L^\eta$ (sorted in increasing order) versus m/L for $\gamma_1 = 1$, $\gamma_2 = -1$, $V_0 = 2.5$, system sizes $L = 3000, 4000, 5000$ and 6000 , and sinusoidal driving. (a) $I_m^{(2)} L^\eta$ for Floquet eigenstates with $\omega = 5$ and $a = 5$. The exponent $\eta = 1$, and we see that all states are extended. (b) $I_m^{(2)} L^\eta$ with $\omega = 40$ and $a = 5$. Here $\eta = 0$ showing that all states are localized. (c) and (d) $I_m^{(2)} L^\eta$ with $\omega = 15.1$ and $a = 5$. Plots (c) and (d) correspond to $\eta = 0$ and 1 respectively, and they clearly show a jump in the IPR value around $m/L \simeq 0.76$. (e) Plot of $I_m^{(2)}$ versus quasienergy E_F for $\omega = 5$, $a = 5$, and $L = 3000$. We see several gaps in E_F .

The results obtained using FPT will be compared with those obtained from an exact numerical calculation of the Floquet operator. To this end, we divide the time period T into N steps so that $H(t)$ does not vary appreciably within the time step $\delta t = T/N$. For the present case, we find that $N \sim 500$ achieves this task; a further increase in N does not change the numerical results appreciably. This allows us to use the standard Suzuki-Trotter decomposition to write U as

$$U(T, 0) = \prod_{j=1, N} U(t_j, t_{j-1}),$$

$$U_j \equiv U(t_j, t_{j-1}) = e^{-iH[(t_j + t_{j-1})/2]\delta t}, \quad (26)$$

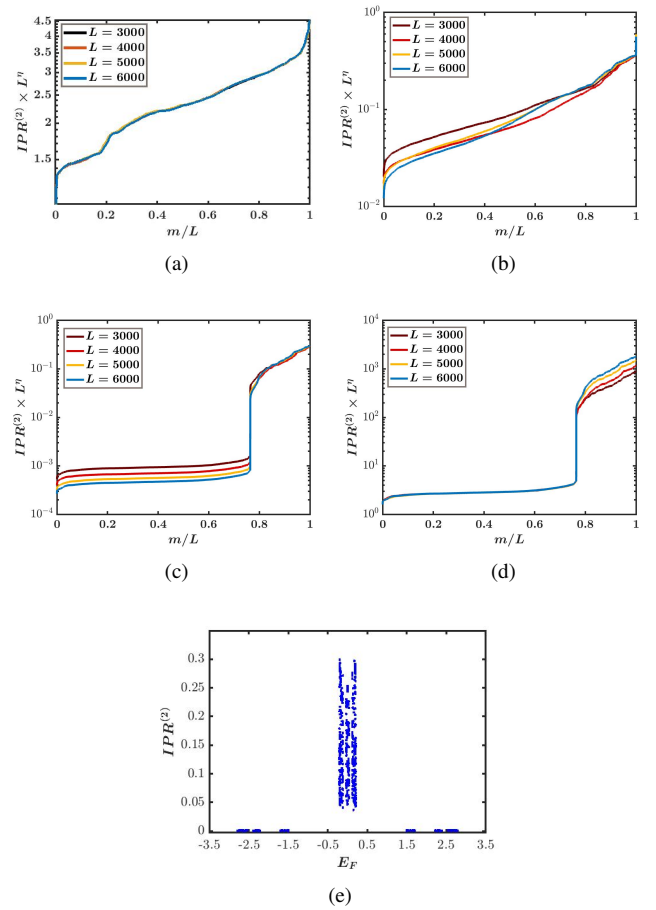


FIG. 2: (a-d) Plots of $I_m^{(2)} L^\eta$ versus m/L and (e) plot of $I_m^{(2)}$ versus E_F for the same parameter values as in Fig. 1 but obtained using first-order FPT. All the plots agree qualitatively with the plots from exact numerics shown in Fig. 1.

where $t_0 = 0$ and $t_N = T$. We can then numerically diagonalize U to obtain its eigenvectors $|\psi_m\rangle$ and eigenvalues $e^{-i\theta_m}$. We can then write

$$U(T, 0) = \sum_m e^{-i\theta_m} |\psi_m\rangle \langle \psi_m|. \quad (27)$$

In this section, we will study and compare the properties of the Floquet eigenstates obtained using first-order FPT and exact numerics. To this end, we compute the inverse participation ratio (IPR) of these eigenstates given, for a normalized Floquet eigenstate m , as

$$I_m^{(2)} = \sum_{j=1}^L |\psi_m(j)|^4. \quad (28)$$

It is well-known that $I_m^{(2)}$ can distinguish between localized and extended states; $I_m^{(2)} \sim L^{-\eta}$ where $\eta = 0$ (1) for localized (extended) eigenstates.

A. Localized, extended and multifractal states

We now present our numerical results. Figures 1 (a-d) show plots of $I_m^{(2)} L^\eta$ (sorted in increasing order) versus m/L for systems with $\gamma_1 = 1$, $\gamma_2 = -1$, $V_0 = 2.5$, different values of ω and a , and sinusoidal driving. For generating this and all subsequent figures, the quasiperiodic potential at site j is taken to be $V_j = V_0 \cos(2\pi\alpha j)$, where α is taken to be a rational approximant for $(\sqrt{5} - 1)/2$ by choosing $\alpha = N/L$, where L is the system size, and N is the integer closest to $L(\sqrt{5} - 1)/2$. We have chosen $L = 3000$, 4000, 5000 and 6000. The plots clearly indicate a jump in the IPR value for certain ranges of values of ω and a . From Figs. 1 (a) and (b), we find that at relatively low (high) driving frequencies, all the Floquet eigenstates are extended (localized). This can be seen from the collapse of the $I_m^{(2)} L^\eta$ curves for $\eta = 1$ at $\omega = 5$ (Fig. 1 (a)) and $\eta = 0$ at $\omega = 40$ (Fig. 1 (b)) for different L . In contrast, at an intermediate driving frequency, $\omega = 15.1$, as shown in Figs. 1 (c) and (d), a jump in the IPR between localized and extended eigenstates around $m/L \simeq 0.76$. The data for different L collapses upon scaling with L^η for two different values of η ; the collapse happens for $\eta = 0$ for $m/L \gtrsim 0.764$ (Fig. 1 (c)) and for $\eta = 1$ for $m/L \lesssim 0.764$ (Fig. 1 (d)). This demonstrates the appearance of an IPR jump around $m/L \simeq 0.76$ at this driving frequency. Figure 1 (e) shows a plot of $I_m^{(2)}$ versus the quasienergy E_F for $\omega = 5$, $a = 5$, and $L = 3000$. This clearly shows that there are gaps in the quasienergy spectrum; we call these mobility gaps. (In this paper, we use the term mobility gap regardless of whether the states in the quasienergy bands on the two sides of a gap are both extended or both localized or one extended and the other localized). The states with E_F around zero have large IPRs and correspond to extended states, whereas states with E_F away from zero (on either the positive or the negative side) have very small IPRs and are localized states. [It is important to note that sorting in increasing order of $I_m^{(2)}$ (as done in Figs. 1 (a-d)) and in increasing order of E_F (as done in Fig. 1 (e)) are completely different from each other. The presence of mobility gaps becomes apparent only in the latter way of sorting].

In Fig. 2, similar plots are shown for Floquet eigenstates obtained from first-order FPT. These correspond to the same parameter values as their counterparts in Fig. 1. A comparison between Figs. 1 and 2 shows that first-order FPT provides a reasonable match to the exact numerics, although the IPR values found from exact numerics are significantly smaller than the ones found from first-order FPT. Importantly, both exact numerics (Fig. 1 (e)) and first-order FPT (Fig. 2 (e)) show mobility gaps at intermediate driving frequencies like $\omega = 5$.

To determine if any of the eigenstates exhibit multifractal behavior, we calculate a generalized IPR defined as

$$I_m^{(q)} = \sum_j |\psi_m(j)|^{2q}, \quad (29)$$

and study its scaling with the system size L .⁴² If $I_m^{(q)}$ scales as $L^{-\eta_q}$ and $\eta_q = (q-1)D_q$, then $D_q = 1$ for all q for

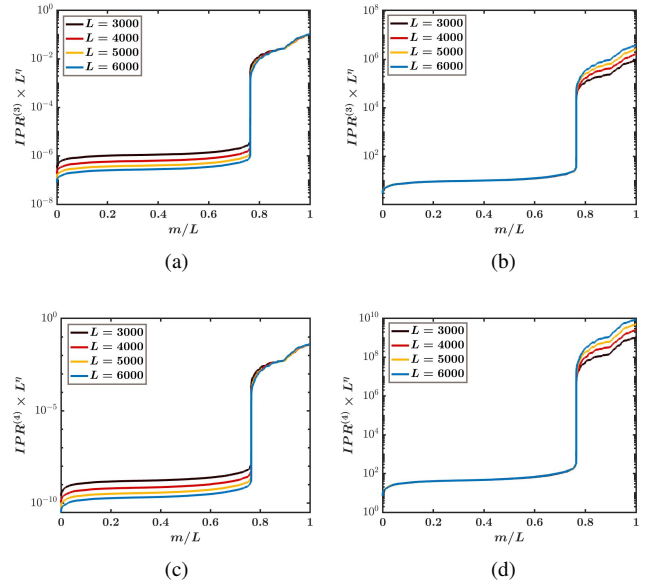


FIG. 3: Plots showing $I_m^{(3)} L^\eta$ and $I_m^{(4)} L^\eta$ (sorted in increasing order) versus m/L obtained by exact numerical calculations for $L = 3000$, 4000, 5000 and 6000, with $\gamma_1 = 1$, $\gamma_2 = -1$, $a = 5$, $\omega = 15.1$, $V_0 = 2.5$, and sinusoidal driving. Plot (a) shows a data collapse of $I_m^{(3)}$ with $\eta = 0$ for $m/L \gtrsim 0.764$. Plot (b) shows a data collapse of $I_m^{(3)}$ with $\eta = 2$ for $m/L \lesssim 0.764$. Plot (c) shows a data collapse of $I_m^{(4)}$ with $\eta = 0$ for $m/L \gtrsim 0.764$. Plot (d) shows a data collapse of $I_m^{(4)}$ with $\eta = 3$ for $m/L \lesssim 0.764$. These plots show that $I_m^{(q)}$ scales with $\eta = 0$ for states with $m/L \gtrsim 0.764$ (localized states) and with $\eta = q-1$ for states with $m/L \lesssim 0.764$ (extended states).

extended states (since $|\psi_m(j)|^2$ is of the order of $1/L$ for all j for such states), and $D_q = 0$ for all q for localized states (since $|\psi_m(j)|^2$ for such states is of order 1 over a finite region whose size remains constant as $L \rightarrow \infty$). Multifractal states typically have $0 < D_q < 1$ for all q . Figure 3 shows plots of $I_m^{(q)} L^\eta$ for $q = 3$ and 4 for systems with $\gamma_1 = 1$, $\gamma_2 = -1$, $\omega = 15.1$, $a = 5$, $V_0 = 2.5$, different system sizes, and sinusoidal driving. Figures 3 (a) and (c) show that states with $m/L \gtrsim 0.764$ scale with L with the powers $\eta_3 = \eta_4 = 0$, showing that $D_q = 0$; hence these states are localized. Figures 3 (b) and (d) show that states with $m/L \lesssim 0.764$ scale with powers $\eta_3 = 2$ and $\eta_4 = 3$, showing that $D_q = 1$; hence these states are extended. Thus there is no evidence of multifractal states for this set of parameter values. However, we will show below that multifractal behavior appears for a different range of values of ω .

In Fig. 4, we show plots of $I_m^{(2)}$ and $I_m^{(3)}$ versus m/L , and their scaling exponents with L , η_2 and η_3 , versus ω and m/L for systems with $\gamma_1 = 1$, $\gamma_2 = -1$, $a = 5$, $V_0 = 2.5$, and sinusoidal driving. Figures 4 (a-b) show $I_m^{(2)}$ and $I_m^{(3)}$ for a system with $L = 3000$, while Figs. 4 (c-d) show the scaling exponents η_2 and η_3 for these two quantities extracted from the results for $L = 3000$, 4000, 5000 and 6000. We see that most states have $\eta_2 = \eta_3 = 0$ (localized) at lower frequencies

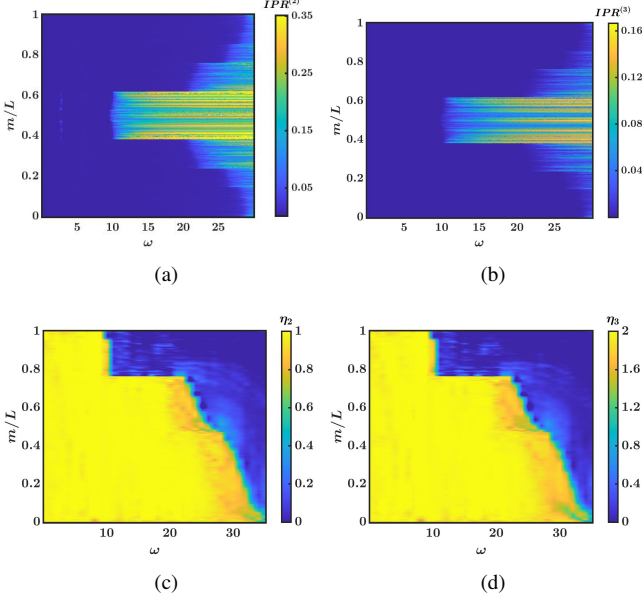


FIG. 4: (a-b) Plots of $I_m^{(2)}$ and $I_m^{(3)}$ (sorted in increasing order of quasienergy) versus ω and m/L for $\gamma_1 = 1$, $\gamma_2 = -1$, $a = 5$, $V_0 = 2.5$, $L = 3000$, and sinusoidal driving. (c-d) Plots of η_2 and η_3 (extracted from the IPRs sorted in increasing order for $L = 3000, 4000, 5000$ and 6000) versus ω and m/L , with the same parameter values as in plots (a-b). Multiple jumps in $I_m^{(2)}$ and $I_m^{(3)}$ observed in plots (a-b) indicate multiple localization-delocalization transitions. This is more evident in plots (c-d) where η_2 and η_3 are extracted from the scaling analysis of $I_m^{(2)}$ and $I_m^{(3)}$ respectively. Note that for $\omega \gtrsim 20$ and $\omega \lesssim 35$ in plots (c-d), the values of η_2 and η_3 for a small fraction of states are different from the usual scaling exponents of extended states (i.e., $\eta_2 = 1$ and $\eta_3 = 2$).

and have $\eta_2 = 1$ and $\eta_3 = 0$ (extended) at higher frequencies. Interestingly, however, we see some states for which η_2 and η_3 are different from the values of both localized and extended states. Hence these states have a multifractal nature. Figure 5 shows similar plots as in Fig. 4 but for square pulse driving. We see almost identical behaviors for the scaling exponents in the two sets of figures. However, the intermediate regions with extended, localized and and multifractal states are somewhat larger in Fig. 5 than in Fig. 4. Figs. 4 and 5 together show that the generation of multifractal states does not depend significantly on the driving protocol.

Figure 6 shows plots of $I_m^{(2)}$ and the scaling exponent η_2 versus ω and m/L for $L = 3000, 4000, 5000$ and 6000 , for $\gamma_1 = \gamma_2 = 1$ (uniform hopping), $a = 5$, $V_0 = 2.5$, and square pulse driving. The results looks somewhat similar to those shown in Fig. 5 for $\gamma_1 = -\gamma_2 = 1$ in that both extended and localized states appear in the two cases. However, extended states persist up to a larger values of ω for $\gamma_1 = -\gamma_2 = 1$ compared to $\gamma_1 = \gamma_2 = 1$.

It is useful to look at the average values of both $I_m^{(2)}$ and the normalized participation ratio (NPR) which, up to a factor of L , is the inverse of $I_m^{(2)}$.⁴⁶ For the m -th Floquet eigenstate, the NPR is defined as $\text{NPR}_m = 1/(L I_m^{(2)})$. The average

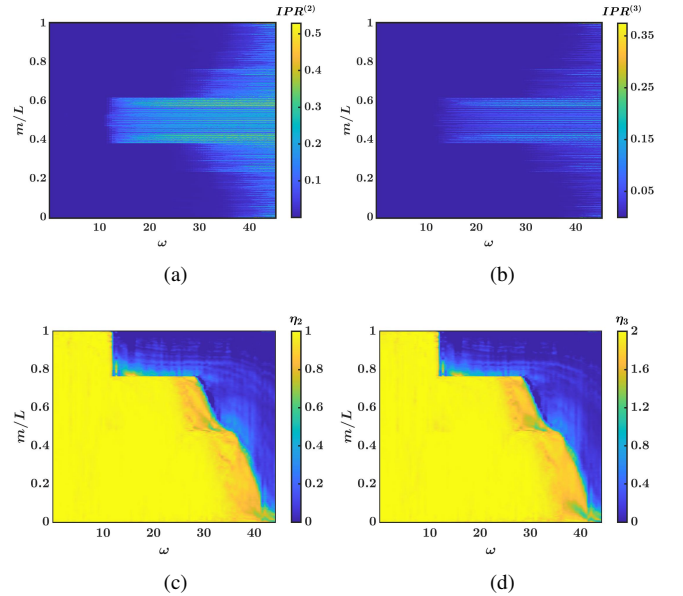


FIG. 5: (a-b) Plots of $I_m^{(2)}$ and $I_m^{(3)}$ (sorted in increasing order of quasienergy) versus ω and m/L for $\gamma_1 = 1$, $\gamma_2 = -1$, $a = 5$, $V_0 = 2.5$, $L = 3000$, and square pulse driving. (c-d) Plots of η_2 and η_3 (extracted from the IPRs sorted in increasing order for $L = 3000, 4000, 5000$ and 6000) versus ω and m/L , with the parameter values same as in plots (a-b). Multiple jumps in $I_m^{(2)}$ and $I_m^{(3)}$ observed in plots (a-b) indicate multiple localization-delocalization transitions. This is more evident in plots (c-d) where η_2 and η_3 are extracted from the scaling analysis of IPR values. We note that for $\omega \gtrsim 30$ and $\omega \lesssim 45$ in plots (c-d), the values of η_2 and η_3 for a small fraction of states are different from the usual scaling exponents of extended states ($\eta_2 = 1$ and $\eta_3 = 2$).

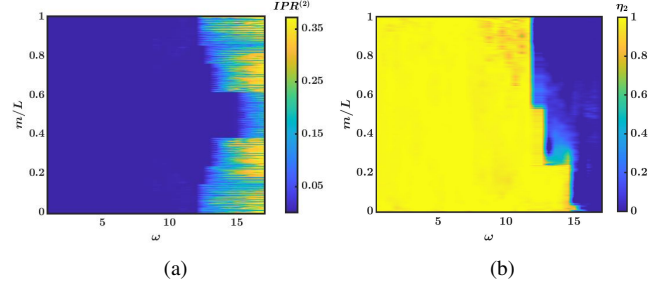


FIG. 6: (a) Plot of $I_m^{(2)}$ (sorted in increasing order of quasienergy) versus ω and m/L with $\gamma_1 = \gamma_2 = 1$ (uniform hopping), $a = 5$, $V_0 = 2.5$, $L = 3000$, and square pulse driving. (b) Plot of η_2 (extracted from the IPRs sorted in increasing order for $L = 3000, 4000, 5000$ and 6000) versus ω and m/L .

values of these two quantities are then defined as $\langle \text{IPR} \rangle = (1/L) \sum_m I_m^{(2)}$ and $\langle \text{NPR} \rangle = (1/L) \sum_m \text{NPR}_m$. For a large system size L , we have $I_m^{(2)} \sim 1/L$ (1) and $\text{NPR}_m \sim 1/(1/L)$ for an extended (localized) state m , respectively. Hence, the quantity $\phi = \log_{10}(\langle \text{IPR} \rangle / \langle \text{NPR} \rangle)$ will be large and negative (of the order of $-\log_{10} L$) either if all states are extended or if all states are localized. But if ϕ is not large and negative, this

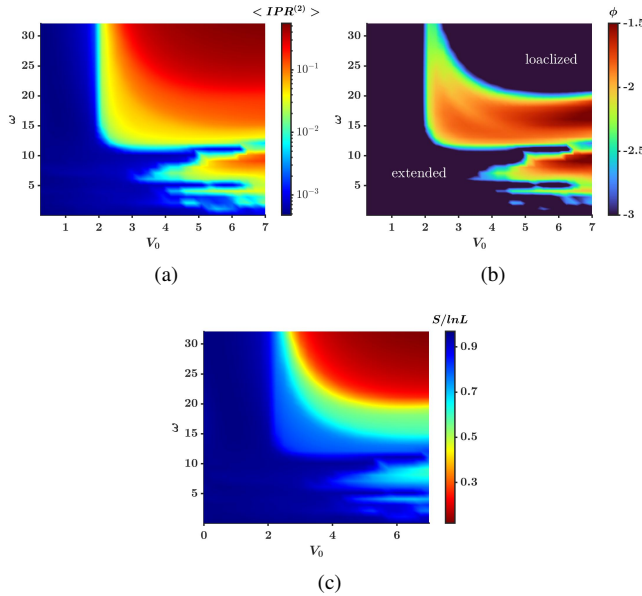


FIG. 7: (a) Plot on a log scale of the average of $I_m^{(2)}$, denoted as $\langle IPR \rangle$, versus V_0 and ω for $\gamma_1 = 1, \gamma_2 = -1, a = 5, L = 3000$, and square pulse driving. (b) Plot of $\phi = \log_{10}(\langle IPR \rangle / \langle NPr \rangle)$ versus V_0 and ω . (c) Plot of the average Shannon entropy $\langle S \rangle$ versus V_0 and ω . Plots (a-c) suggest that all the Floquet eigenstates below $V_0 \simeq 2$ are extended for all values of ω . For $2 \lesssim V_0 \lesssim 3.5$, we find three distinct regions, with only extended states for small ω , multifractal states for intermediate ω , and only localized states for large ω . A different behavior appears for $V_0 \gtrsim 3.5$, where we see multiple re-entrant transitions between regions with only extended and only localized states as ω is increased.

would indicate that there are some states which are neither extended nor localized. We will also look at the average value of the Shannon entropy as another measure of the degree of localization²³. For the m -th Floquet eigenstate, the Shannon entropy is defined as $S_m = -\sum_n |\psi_m(n)|^2 \ln(|\psi_m(n)|^2)$, and its average is then given by $\langle S \rangle = (1/L) \sum_m S_m$. For an extended (localized) state m , we have $S_m \sim \ln L$ (0), respectively. Hence the average value $\langle S \rangle$ will be of order $\ln L$ if all states are extended and will be close to zero if all states are localized.

Figure 7 shows plots of $\langle IPR \rangle$, $\phi = \log_{10}(\langle IPR \rangle / \langle NPr \rangle)$, and $\langle S \rangle$ versus ω and V_0 , for a system with $\gamma_1 = 1, \gamma_2 = -1, a = 5$ and square pulse driving. Figure 7 (a) indicates that all states are extended when both ω and V_0 are small and are localized when both ω and V_0 are large. For $2 \lesssim V_0 \lesssim 3.5$, we see that only extended states for low values of ω , multifractal states for intermediate values of ω , and only localized states for large values of ω . Interestingly, when $V_0 \gtrsim 3.5$, we find multiple re-entrant transitions between regions with only extended and only localized states as ω is increased. These observations are confirmed qualitatively by Figs. 7 (b) and (c).

Figure 8 shows plots of $I_m^{(2)}$, the scaling exponent η_2 and the real part of the Floquet eigenvalues versus ω and m/L for systems with $\gamma_1 = 1, \gamma_2 = -1, a = 5, V_0 = 5.5$ and different sizes, for square pulse driving. This figure confirms the mul-

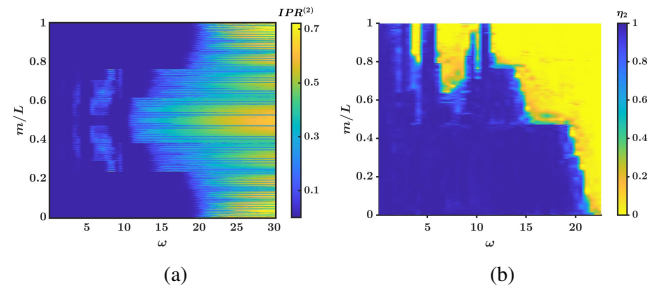


FIG. 8: (a) Plot of $I_m^{(2)}$ (sorted in increasing order of quasienergy) versus ω and m/L , with $\gamma_1 = 1, \gamma_2 = -1, a = 5, V_0 = 5.5, L = 3000$, and square pulse driving. (b) Plot of η_2 versus ω and m/L . We extract η_2 using system sizes $L = 3000, 4000, 5000$ and 6000 . The plots confirm the multiple transitions seen in Fig. 7 for $V_0 \gtrsim 3.5$ as ω is varied. Plot (b) shows several transitions. A transition to a phase with all extended states occurs at $\omega \simeq 5.1$, and this phase then continues up to $\omega \simeq 7.1$. For $\omega \gtrsim 7.1$, we get both extended and localized states till $\omega \simeq 9.1$. Another phase of extended states appears for $9.2 \lesssim \omega \lesssim 12.1$. Beyond $\omega \simeq 12.1$, plot (b) suggests that the system moves towards complete localization as ω increases.

multiple re-entrant transitions between regions which are completely extended, completely localized, or have both extended and localized states, that we see in Fig. 7 when $V_0 \gtrsim 3.5$. (We note that similar re-entrant transitions have been observed in a kicked quasicrystal⁴⁹).

Figure 9 shows plots of $IPR^{(2)}$ and the scaling exponent η_2 versus ω for systems with $\gamma_1 = 1, \gamma_2 = -1, a = 5, V_0 = 2.5$ and different sizes, as obtained using first-order FPT for both sinusoidal and square pulse driving. The plots look similar for the two driving protocols.

Fig. 10 shows the average $\langle IPR \rangle$ and average Shannon entropy $\langle S \rangle$ as functions of V_0 and of ω for a system with uniform hopping, $\gamma_1 = \gamma_2 = 1, a = 5$ and $L = 3000$, for square pulse driving. The results deviate significantly from the case of staggered hopping, $\gamma_2 = -\gamma_1$, shown in Fig. 7, particularly for $V_0 \gtrsim 3.5$.

B. High-frequency limit

In the high-frequency limit $\omega \gg a \gg \gamma_1, \gamma_2, V_0$, we expect the effects of driving to disappear as we have argued in Sec. II. Surprisingly, however, we find that although the quasienergies for large ω match the energies for the undriven system, the IPRs do not agree in the two cases.

In Figs. 11 (a) and (b), we show plots of $I_m^{(2)}$ versus quasienergy E_F (sorted in increasing order) for systems with $\gamma_1 = 1, \gamma_2 = -1$ and $+1$ respectively, $\omega = 35, a = 5, V_0 = 2.5, L = 3000$, and square pulse driving. Fig. 11 (c) shows a plot of $I_m^{(2)}$ versus energy E (sorted in increasing order) for an undriven system with $\gamma_1 = 1, \gamma_2 = 1$ (the relative sign of γ_1 and γ_2 is unimportant in the absence of driving), $V_0 = 2.5$, and $L = 3000$. We have chosen $V_0 = 2.5$ so that $V_0 > 2\gamma_1$ and all the states of the undriven system are

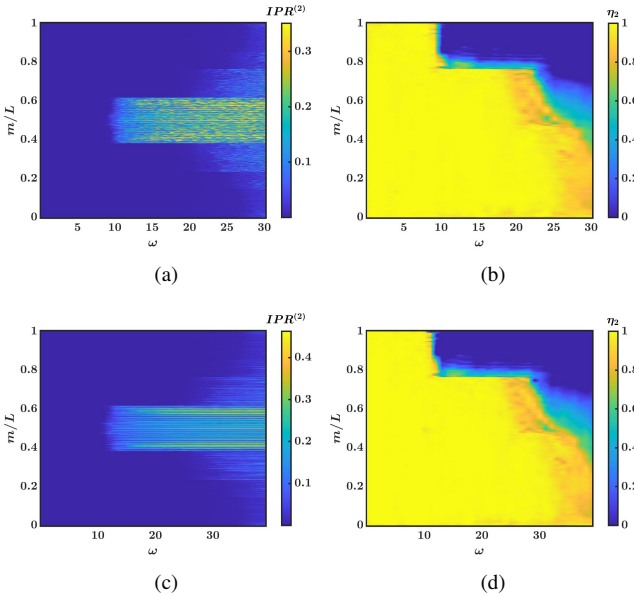


FIG. 9: (a) and (c) Plots of $I_m^{(2)}$ (sorted in increasing order of quasienergy) versus ω and m/L , for $\gamma_1 = 1$, $\gamma_2 = -1$, $a = 5$, $V_0 = 2.5$, and $L = 3000$, obtained using first-order FPT. (b) and (d) Plots of η_2 versus ω and m/L . System sizes $L = 3000, 4000, 5000$ and 6000 were used to extract the values of η_2 . Plots (a-b) and (c-d) are for sinusoidal and square pulse drivings respectively.

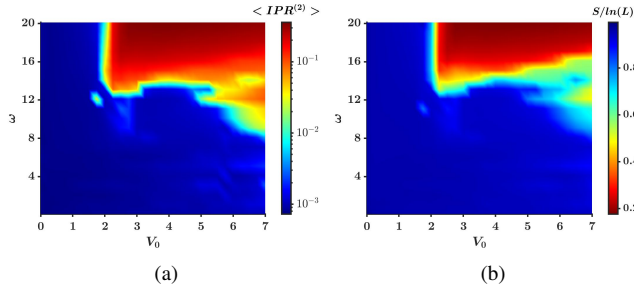


FIG. 10: (a) Plot on a log scale of the average of $I_m^{(2)}$, $\langle \text{IPR} \rangle$, versus ω and V_0 , with $\gamma_1 = \gamma_2 = 1$ (uniform hopping), $a = 5$, $L = 3000$, and square pulse driving. (b) Plot of average Shannon entropy, $\langle S \rangle$, versus ω and V_0 . For $V_0 \gtrsim 3.5$, we see that the case of uniform hopping shown here deviates significantly from the case of non-uniform hopping shown in Fig. 7.

localized. We note that the quasienergies in plots (a) and (b) and the energies in plot (c) have almost the same values. This is expected since driving at high frequencies should give the same Floquet Hamiltonian as the undriven part of the Hamiltonian. Surprisingly, however, the IPR values are not the same in the three plots. The IPR values for the driven system with uniform hopping amplitudes differ only a little from the IPRs of the undriven system, but the IPRs of the driven staggered model ($\gamma_2 = -\gamma_1$) differ substantially from those of the undriven system. (This may be because driving has a smaller effect when $\gamma_2 = \gamma_1$ compared to $\gamma_2 = -\gamma_1$, for reasons explained after Eq. (17)). We observe that the undriven system

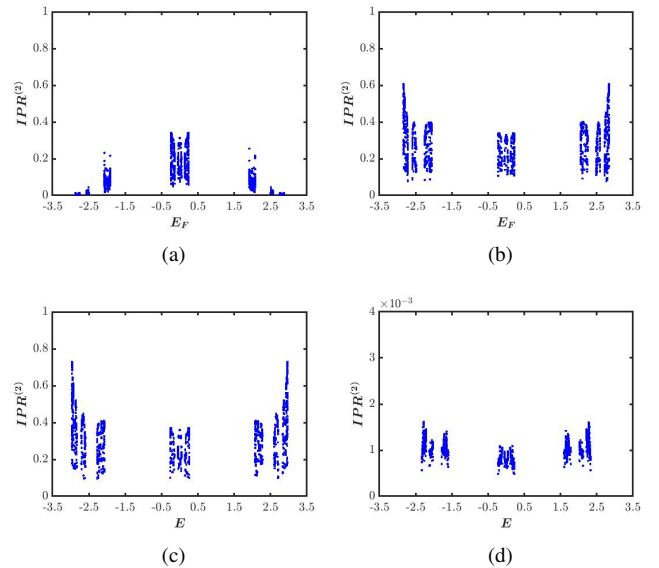


FIG. 11: (a) Plot of $I_m^{(2)}$ versus quasienergy E_F (sorted in increasing order) for a system with $\gamma_1 = 1$, $\gamma_2 = -1$, $\omega = 35$, $a = 5$, $V_0 = 2.5$, $L = 3000$, and square pulse driving. (b) Plot of $I_m^{(2)}$ versus quasienergy for a system with $\gamma_1 = 1$, $\gamma_2 = 1$ (uniform hopping), $\omega = 35$, $a = 5$, and $V_0 = 2.5$. (c) Plot of $I_m^{(2)}$ versus energy E (sorted in increasing order) for an undriven system ($a = 0$) with $\gamma_1 = 1$, $\gamma_2 = 1$, and $V_0 = 2.5$. (d) Plot of $I_m^{(2)}$ versus energy E (sorted in increasing order) for an undriven system ($a = 0$) with $\gamma_1 = 1$, $\gamma_2 = -1$, and $V_0 = 1.5$. Note that the range of IPR values in plot (d) is much smaller than in plots (a-c). In all cases we have considered system size $L = 3000$ and square pulse driving.

(plot (c)) shows only localized states, but the driven staggered model (plot (a)) shows that some of the states have very low IPR values and are therefore extended states. Thus driving even at a high frequency seems to convert some of the localized states to extended states, provided that $a \gg \gamma_1$, γ_2 and V_0 . (We have checked numerically that if $a \ll \gamma_1$, γ_2 and V_0 , then all the states remain localized). This suggests that although terms of order $1/\omega$ and higher in the Floquet Hamiltonian are small for large ω , they have a significant effect on the IPR values of the Floquet eigenstates. It is possible that these small terms have a negligible effect on the quasienergies, but they couple localized states which lie close to each other and this hybridization produces extended states.

On the other hand, if we choose $V_0 < 2\gamma_1$ and all the other parameters are the same as in Figs. 11 (a-c), we find that there is no discernible differences between the spectra of quasienergies (or energies) and IPR values in the three cases. All the states are extended in all three cases (driven with $\gamma_2 = \pm\gamma_1$ and undriven). Fig. 11 (d) shows a plot of the energies and corresponding IPR values for an undriven system with $\gamma_1 = 1$, $\gamma_2 = -1$, and $V_0 = 1.5$. The IPR versus quasienergy plots for the driven systems with $\gamma_2 = \pm\gamma_1$ look the same and are not shown here.

In Fig. 12, we show plots of all the quasienergies E_{Fm} for systems with $\gamma_1 = 1$, $\gamma_2 = -1$, $a = 5$, size $L = 2000$,

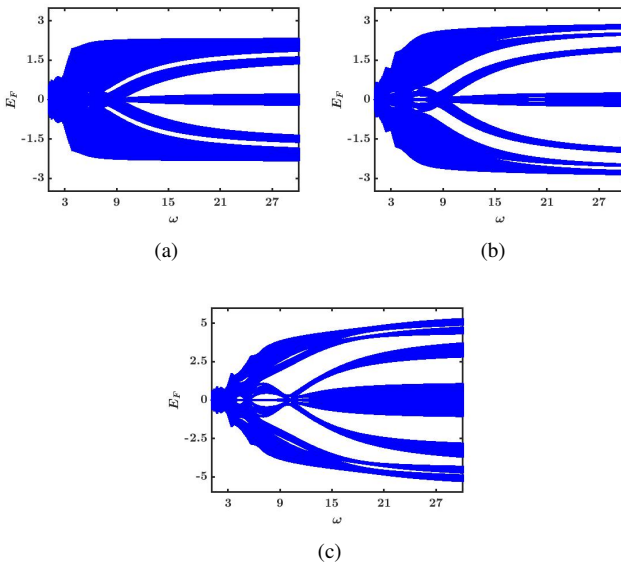


FIG. 12: Plots of E_{Fm} versus ω for (a) $V_0 = 1.5$, (b) $V_0 = 2.5$, and (c) $V_0 = 5.5$, for systems with $\gamma_1 = 1$, $\gamma_2 = -1$, $a = 5$, size $L = 2000$, and square pulse driving. The spectrum of E_{Fm} is gapless for intermediate ω and develops several gaps as ω increases.

square pulse driving, and (a) $V_0 = 1.5$, (b) $V_0 = 2.5$, and (c) $V_0 = 5.5$. (We note that E_{Fm} is found from the eigenvalues $e^{-i\theta_m}$ of the Floquet operator as $E_{Fm} = \theta_m/T$. Hence E_{Fm} lies in the range $[-\omega/2, \omega/2]$). These plots show that the spectrum of E_{Fm} is generally gapless for intermediate frequencies but several gaps appear as ω is increased. This can be qualitatively understood from the FPT as follows. In the limit that $\gamma_1, \gamma_2, V_0 \ll \omega \ll a$, we saw in the discussion given towards the end of Sec. II that the model reduces to one in which the hopping amplitude is uniform and the quasiperiodic potential is absent. This system clearly has no gaps in the spectrum.

On the other hand, when $\gamma_1, \gamma_2, V_0 \ll a \ll \omega$, we saw that the model reduces to an undriven system ($a = 0$). Hence the quasienergies will approach the energies of the undriven system. For the undriven Aubry-André model, it is known that there is a large number (in fact, an infinite number) of energy gaps for any non-zero value of V_0 .^{44,45} It would be useful to understand precisely how the different gaps appear successively as ω is increased from intermediate to large values. [We have checked numerically that for $V_0 = 0$, there are no gaps for any value of ω or a . Hence the gaps are appearing only because a quasiperiodic potential is present].

C. Floquet Hamiltonian in real space

To visualize the effects of localization, it is instructive to look at the matrix elements of the Floquet Hamiltonian. Figure 13 shows the absolute values of the matrix elements of $H_F(X, Y)$ in real space for systems with $\gamma_1 = 1$, $\gamma_2 = -1$, $V_0 = 2.5$, size $L = 2000$, and sinusoidal driving. $H_F(X, Y)$ is obtained by doing a Fourier transform of H_F in momentum space as found numerically from the Floquet operator U (Figs. 13 (a-c)) or from the first-order FPT (Figs. 13 (d-f)) given in Sec. II. The plots are shown as a function of $Y - X$ and X . If the system was translation invariant, the plot would depend only on the relative coordinate $Y - X$ and not on X . Indeed we see that the plots do not vary with X at length scales much larger than $1/\beta \simeq 1.62$ (which is the length scale of variation of the quasiperiodic potential $\cos(2\pi\beta j)$). In terms of the relative coordinate $Y - X$, the plots show a large spread in Figs. 13 (a) and (d) corresponding to all states being extended, a smaller spread in Figs. 13 (b) and (e) corresponding to a case where there are both localized and extended states, and a very small spread in Figs. 13 (c) and (f) corresponding to all states being extended.

D. Spreading of a one-particle wave packet

We now consider a measure of delocalization given by the spreading of a one-particle state which is initially localized at the middle site of system of size L , namely, the site $j_0 = L/2$. This initial state, denoted $|\psi_{in}\rangle$, is evolved over n time periods by acting on it with the Floquet operator n times. This gives

$$|\psi_{nT}\rangle = U^n |\psi_{in}\rangle. \quad (30)$$

The root mean squared displacement is then given by

$$\sigma(n) = \left[\sum_j (j - j_0)^2 |\psi_{nT}(j)|^2 \right]^{1/2}. \quad (31)$$

The growth of $\sigma(n)$ with n gives an idea of how delocalized the system is. Fig. 14 shows plots of $\sigma(n)$ for systems with

$\gamma_1 = 1$, $\gamma_2 = \pm 1$ (uniform and staggered hopping amplitudes respectively), $a = 5$, $\omega = 5$ and 30 , various values of V_0 , and square pulse driving. (The system size L is taken to be 6000). We see that the spreading of the wave packet is always ballistic. The ballistic velocity, given by the slope of $\sigma(n)$ versus n , is smaller for $\omega = 30$ compared to $\omega = 5$. This is because driving with a very large frequency is equivalent to not driving at all. In the absence of driving, it is known that a system with a quasiperiodic potential with strength $V_0 < 2\gamma_1$ has only extended states, while a system with $V_0 > 2\gamma_1$ has only localized states^{44,45}; these results hold regardless of whether $\gamma_2 = \gamma_1$ or $\gamma_2 = -\gamma_1$ since we can change the sign of γ_2 by doing a unitary transformation which does not affect γ_1 and V_0 . Indeed we see in Figs. 14 (b) and (d), that the wave packet spreads ballistically if $V_0 < 2$ but remains completely localized if $V_0 > 2$. The situation at the lower frequency, $\omega = 5$, is more interesting. The system with staggered hop-

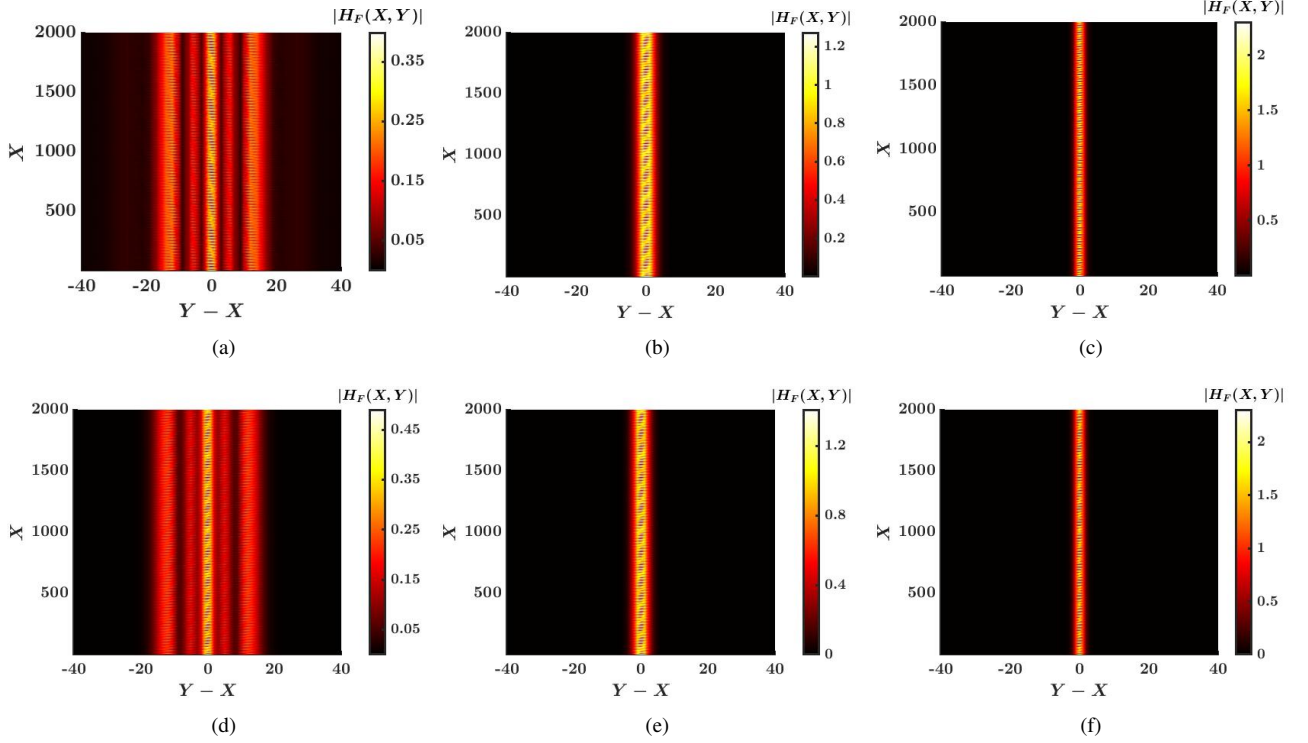


FIG. 13: Plots of the absolute values of the matrix elements of the Floquet Hamiltonian $H_F(X, Y)$ in real space (X and Y represent space coordinates), where the axes are chosen to be X and $Y - X$. In all cases, we considered $\gamma_1 = 1$, $\gamma_2 = -1$, $V_0 = 2.5$, system size $L = 2000$, and sinusoidal driving. Figures (a-c) are obtained from exact numerical calculations. The parameters used are (a) $a = 10$, $\omega = 5$, (b) $a = 5$, $\omega = 15.1$, and (c) $a = 5$, $\omega = 40$. In contrast, figures (d-f) are obtained from the first-order FPT. The parameter values for these figures are (d) $a = 10$, $\omega = 5$, (e) $a = 5$, $\omega = 15.1$, and (f) $a = 5$, $\omega = 40$. The two sets of figures, one obtained from the exact numerics and the other from first-order FPT, agree well with each other. We note that plots (a) and (d) are for a system with only extended states, plots (b) and (e) are for a system with both extended and localized states, and plots (c) and (f) are for a system with only localized states.

ping, $\gamma_2 = -\gamma_1$, shows ballistic spreading for $V_0 = 1.5, 3$ and 6 , and no spreading for $V_0 = 9$. However, the system with uniform hopping, $\gamma_2 = \gamma_1$, always shows some ballistic spreading for all values of V_0 . Further, the ballistic velocity is a non-monotonic function of V_0 , being smaller for $V_0 = 1.5$ and 9 compared to $V_0 = 3$ and 6 . A similar non-monotonic behavior of the ballistic spreading is seen in Fig. 15 for driving at an intermediate frequency with $\omega = 12$.

IV. PERTURBATION THEORY FOR A MODEL WITH UNIFORM HOPPING

In this section we will study a system with a uniform hopping amplitude, $\gamma_1 = \gamma_2 = 1$, which is driven by a square pulse. For uniform hopping, the unit cell consists of a single site and we will denote the fermionic operator as c_j . The Hamiltonian is given by

$$H(t) = (1 + f(t)) \sum_j (c_j^\dagger c_{j+1} + \text{H.c.}) + V_0 \sum_j \cos(2\pi\beta j) c_j^\dagger c_j, \quad (32)$$

where $f(t)$ has the square pulse form described in Eq. (21). Note that for $V_0 = 0$, the periodic driving would have no effect since the time-independent and driven parts of the Hamiltonian commute with each other in that case, and the Floquet Hamiltonian H_F would just be given by $\sum_j (c_j^\dagger c_{j+1} + \text{H.c.})$ independently of the driving frequency.

We will now find the Floquet Hamiltonian H_F in the high-frequency regime using van Vleck perturbation theory^{4,6}. This is a perturbative expansion in powers of $1/\omega$, and it has the advantage over the Floquet-Magnus expansion that it does not depend on the phase of the driving protocol, i.e., it is invariant under $f(t) \rightarrow f(t + t_0)$. Further, unlike the FPT which gives us H_F in momentum space, the van Vleck perturbation theory gives us H_F in real space. This makes it more suitable for studying the dynamics of a wave packet.

The zeroth-order Floquet Hamiltonian given by van Vleck perturbation theory turns out to be

$$\begin{aligned} H_F^{(0)} &= \frac{1}{T} \int_0^T dt H(t) \\ &= \sum_j (c_j^\dagger c_{j+1} + \text{H.c.}) + V_0 \sum_j \cos(2\pi\beta j) c_j^\dagger c_j. \end{aligned} \quad (33)$$

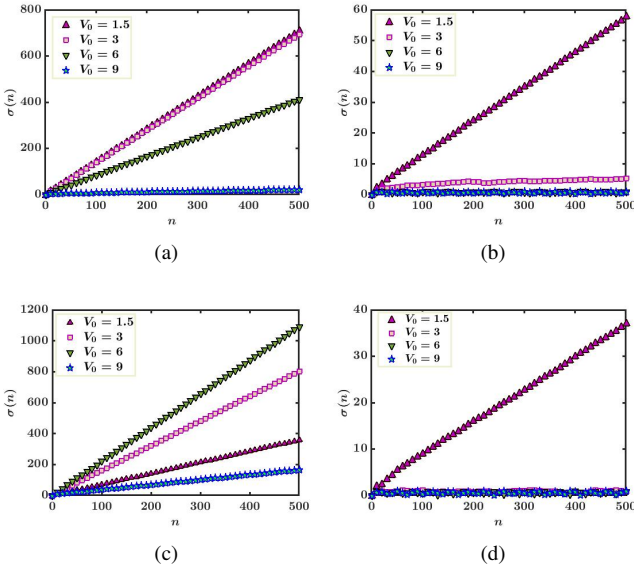


FIG. 14: (a-b) Root mean squared displacement, $\sigma(n)$, versus the stroboscopic evolution number n for $\gamma_1 = 1$, $\gamma_2 = -1$, $a = 5$, and $\omega = 5$ and $\omega = 30$ respectively, for a one-particle state which is initially located at the middle site of a large system. (c-d) Plot of $\sigma(n)$ versus n for $\gamma_1 = \gamma_2 = 1$ (uniform hopping), $a = 5$, and $\omega = 5$ and $\omega = 30$, respectively. All the figures are for system size $L = 6000$ and square pulse driving. Plots (a-b) show that compared to the high-frequency regime (where the behavior is similar to an un-driven system), the intermediate-frequency regime shows a ballistic behavior up to a larger value of V_0 for the case of staggered hopping compared to uniform hopping. For the uniform hopping system at the lower value of $\omega = 5$, plot (c) exhibits a non-monotonic ballistic velocity of $\sigma(n)$ as a function of V_0 before showing a completely localized behavior for large V_0 . Such a non-monotonic behavior is not seen at the higher value of $\omega = 30$ as shown in plot (d).

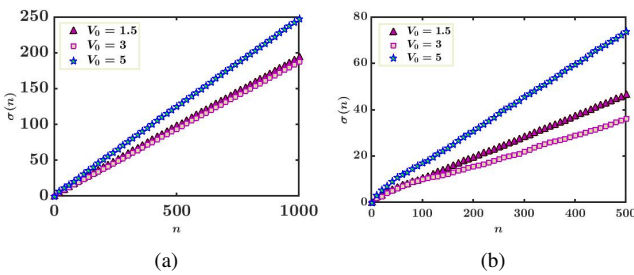


FIG. 15: (a) Root mean squared displacement, $\sigma(n)$, versus the stroboscopic evolution number n from the exact numerical calculation with $\gamma_1 = \gamma_2 = 1$ (uniform hopping), $a = 5$, and $\omega = 12$. (b) $\sigma(n)$ versus n as obtained from the second-order Floquet Hamiltonian in Sec. IV. Both figures are for $L = 3000$ and square pulse driving. The two figures agree qualitatively and indicate a non-monotonic ballistic velocity of $\sigma(n)$ as V_0 increases.

The m -th Fourier component of $H(t)$ is given by

$$H_m = \frac{2ia}{m\pi} \sum_j (c_j^\dagger c_{j+1} + \text{H.c.}) \text{ for } m \text{ odd,} \\ = 0 \text{ for } m \text{ even and } \neq 0, \quad (34)$$

and $H_0 = H_F^{(0)}$. We then find that the first-order Floquet Hamiltonian, $H_F^{(1)} = \sum_{m \neq 0} [H_{-m}, H_m] / (2m\omega)$, is zero since $H_{-m} = (-1)^m H_m$ for all m . The second-order Floquet Hamiltonian consists of two terms

$$H_F^{(2)} = \sum_{m \neq 0} \frac{[[H_{-m}, H_0], H_m]}{2m^2\omega^2} \\ + \sum_{m \neq 0} \sum_{n \neq 0} \frac{[[H_{-m}, H_{m-n}], H_n]}{3mn\omega^2}. \quad (35)$$

The first term in Eq. (35) takes the form

$$H_F^{(2)} = 2t_2 \sum_j [\cos(2\pi\beta(j+1)) + \cos(2\pi\beta(j-1)) \\ - 2\cos(2\pi\beta j)] c_j^\dagger c_j \\ + t_2 \sum_j [2\cos(2\pi\beta(j+1)) - \cos(2\pi\beta(j+2)) \\ - \cos(2\pi\beta j)] (c_j^\dagger c_{j+2} + \text{H.c.}), \quad (36)$$

where $t_2 = a^2 T^2 V_0 / 96$. The second term in Eq. (35) turns out to be zero. The third-order Floquet Hamiltonian vanishes due to the symmetry given in Eq. (24). In principle we can calculate higher order terms but such corrections are expected to be small compared to $H_F^{(0)}$ and $H_F^{(2)}$.

Fig. 15 shows a comparison between the results obtained for the root mean squared displacement $\sigma(n)$ versus the stroboscopic evolution number n as obtained from exact numerics and the second-order Floquet Hamiltonian derived above, for systems with $a = 5$, $\omega = 12$, various values of V_0 , and square pulse driving. We find a qualitative agreement between the two sets of results.

V. DISCUSSION

We now summarize our results. We considered a one-dimensional model with time-independent staggered hopping amplitudes γ_1 and γ_2 and a periodically driven uniform hopping amplitude between nearest-neighbor sites, and a quasiperiodic potential with strength V_0 . We have studied the effects of both sinusoidal driving and driving by a periodic square pulse. While we have mainly studied the case of staggered hopping amplitudes, $\gamma_2 = -\gamma_1$, we have also looked at the case with uniform hopping amplitudes, $\gamma_2 = \gamma_1$, for comparison. In the limit that the driving amplitude a and frequency ω are much larger than γ_1 , γ_2 and V_0 , a Floquet Hamiltonian H_F was analytically derived to first-order in Floquet perturbation theory. Next, the Floquet operator U was

calculated numerically. The eigenstates and eigenvalues of U were found, and various properties of the Floquet eigenstates were then examined as follows.

We studied a generalized IPR, called $I_m^{(q)}$, of the Floquet eigenstates (labeled as m), and found the exponent of their scaling with the system size L , namely, $I_m^{(q)} \sim 1/L^{\eta_q}$. For standard extended states we expect $\eta_q = q - 1$ for all q , while standard localized states have $\eta_q = 0$ for all q . We found that while most states are either extended or localized in a standard way, there are some multifractal states which show an intermediate behavior with $0 < \eta_q < q - 1$ (we have looked at the cases $q = 2, 3$ and 4). These states typically appear at intermediate frequencies ω and large values of V_0 . A study of the average Shannon entropy also suggests that there are three kinds of states, extended, localized and multifractal.

Interestingly, we find that in the high-frequency limit where ω is much larger than all the other parameters, γ_1, γ_2, V_0 and a , the quasienergies are almost the same as the energies for the undriven system ($a = 0$), but the corresponding IPRs can have quite different values when V_0 is large and $\gamma_2 = -\gamma_1$. Namely, when V_0 is larger than the critical value $2\gamma_1$, we know that all the states of the undriven system are localized. We then find that periodic driving of this system at a high frequency does not change the spectrum of quasienergies noticeably but significantly reduces some of the IPR values. Thus driving seems to convert some of the localized states to extended states. The exact mechanism by which this happens may be an interesting problem for future studies.

In general, our numerical results show that there are many gaps in the quasienergy which separate states with significantly different values of the IPR (see Figs. 1 (e) and 2 (e) in particular). These mobility gaps appear due to the presence of the quasiperiodic potential. The number of gaps increases as the driving frequency is increased from intermediate to large

values, as we see in Fig. 12. It would be useful to study exactly why this happens. Interestingly, our numerical results show only mobility gaps. We have not found any examples of mobility edges which appear when there is a continuous range of quasienergies, and somewhere within that range there is a particular quasienergy which separates localized and extended states.

As a dynamical signature of localization, we have studied how a one-particle state initialized at one particular site of the system evolves in time. For all the parameter values that we have examined, we find that the mean squared displacement always increases linearly in time. The ballistic velocity, given by the slope of the displacement versus time, depends on the system parameters. The velocity generally decreases as either ω or V_0 is increased. However, for a system with uniform hopping amplitudes ($\gamma_2 = \gamma_1$) and intermediate values of ω , the velocity shows a non-monotonic dependence on V_0 .

There is some evidence of re-entrant transitions in a recent experiment in which ultracold bosonic atoms are trapped in an optical lattice and the atoms experience a quasiperiodic potential whose strength is given periodic δ -function kicks⁴⁹. The experiment finds regimes of parameter space where there are multiple transitions between localized, extended and multifractal states as the strength of the kicked quasiperiodic potential is varied.

Acknowledgments

S.A. thanks MHRD, India for financial support through a PMRF. K.S. thanks DST, India for support through SERB project JCB/2021/000030. D.S. thanks SERB, India for funding through Project No. JBR/2020/000043.

¹ S. Blanes, F. Casas, J. A. Oteo, and J. Ros, Physics Reports **470**, 151 (2009).

² S. N. Shevchenko, S. Ashhab, and F. Nori, Physics Reports **492**, 1 (2010).

³ L. D'Alessio and A. Polkovnikov, Ann. Phys. **333**, 19 (2013).

⁴ M. Bukov, L. D'Alessio and A. Polkovnikov, Adv. Phys. **64**, 139 (2015).

⁵ L. D'Alessio, Y. Kafri, A. Polkovnikov, and M. Rigol, Adv. Phys. **65**, 239 (2016).

⁶ T. Mikami, S. Kitamura, K. Yasuda, N. Tsuji, T. Oka, and H. Aoki, Phys. Rev. B **93**, 144307 (2016).

⁷ T. Oka and S. Kitamura, Annu. Rev. Condens. Matter Phys. **10**, 387 (2019).

⁸ S. Bandyopadhyay, S. Bhattacharjee and D. Sen, J. Phys. Condens. Matter **33**, 393001 (2021); A. Sen, D. Sen, and K. Sengupta, J. Phys. Condens. Matter **33**, 443003 (2021).

⁹ T. Kitagawa, E. Berg, M. Rudner, and E. Demler, Phys. Rev. B **82**, 235114 (2010); T. Kitagawa, T. Oka, A. Brataas, L. Fu, and E. Demler, Phys. Rev. B **84**, 235108 (2011).

¹⁰ N. H. Lindner, G. Refael, and V. Galitski, Nat. Phys. **7**, 490 (2011).

¹¹ M. Thakurathi, A. A. Patel, D. Sen, and A. Dutta, Phys. Rev. B **88**, 155133 (2013); M. Thakurathi, K. Sengupta, and D. Sen, Phys. Rev. B **89**, 235434 (2014).

¹² A. Kundu, H. A. Fertig, and B. Seradjeh, Phys. Rev. Lett. **113**, 236803 (2014).

¹³ F. Nathan and M. S. Rudner, New J. Phys. **17**, 125014 (2015).

¹⁴ B. Mukherjee, A. Sen, D. Sen, and K. Sengupta, Phys. Rev. B **94**, 155122 (2016); B. Mukherjee, P. Mohan, D. Sen, and K. Sengupta, Phys. Rev. B **97**, 205415 (2018).

¹⁵ V. Khemani, A. Lazarides, R. Moessner, and S. L. Sondhi, Phys. Rev. Lett. **116**, 250401 (2016).

¹⁶ D. V. Else, B. Bauer, and C. Nayak, Phys. Rev. Lett. **117**, 090402 (2016).

¹⁷ J. Zhang, P. W. Hess, A. Kyprianidis, P. Becker, A. Lee, J. Smith, G. Pagano, I.-D. Potirniche, A. C. Potter, A. Vishwanath, N. Y. Yao, and C. Monroe, Nature (London) **543**, 217 (2017).

¹⁸ A. Russomanno, A. Silva, and G. E. Santoro, Phys. Rev. Lett. **109**, 257201 (2012).

¹⁹ A. Lazarides, A. Das, and R. Moessner, Phys. Rev. E **90**, 012110 (2014).

²⁰ T. Nag, S. Roy, A. Dutta, and D. Sen, Phys. Rev. B **89**, 165425 (2014); T. Nag, D. Sen, and A. Dutta, Phys. Rev. A **91**, 063607 (2015).

²¹ A. Agarwala, U. Bhattacharya, A. Dutta, and D. Sen, Phys. Rev. B **93**, 174301 (2016); A. Agarwala and D. Sen, Phys. Rev. B **95**, 014305 (2017).

²² D. J. Luitz, Y. Bar Lev, and A. Lazarides, SciPost Phys. **3**, 029 (2017); D. J. Luitz, A. Lazarides, and Y. Bar Lev, Phys. Rev. B **97**, 020303(R) (2018).

²³ R. Ghosh, B. Mukherjee, and K. Sengupta, Phys. Rev. B **102**, 235114 (2020).

²⁴ A. Das, Phys. Rev. B **82**, 172402 (2010); S. Bhattacharyya, A. Das, and S. Dasgupta, Phys. Rev. B **86**, 054410 (2012); S. S. Hegde, H. Katiyar, T. S. Mahesh, and A. Das, Phys. Rev. B **90**, 174407 (2014).

²⁵ S. Mondal, D. Pekker, and K. Sengupta, Europhys. Lett. **100**, 60007 (2012); U. Divakaran and K. Sengupta, Phys. Rev. B **90**, 184303 (2014).

²⁶ S. Lubini, L. Chirundojan, G.-L. Oppo, A. Politi, and P. Politi, Phys. Rev. Lett. **122**, 084102 (2019).

²⁷ M. Heyl, A. Polkovnikov, and S. Kehrein, Phys. Rev. Lett. **110**, 135704 (2013).

²⁸ A. Sen, S. Nandy, and K. Sengupta, Phys. Rev. B **94**, 214301 (2016); S. Nandy, K. Sengupta, and A. Sen, J. Phys. A: Math. Theor. **51**, 334002 (2018).

²⁹ For a review, see M. Heyl, Rep. Prog. Phys. **81**, 054001 (2018).

³⁰ C. Karrasch and D. Schuricht, Phys. Rev. B **87**, 195104 (2013).

³¹ J. N. Kriel and C. Karrasch, and S. Kehrein, Phys. Rev. B **90**, 125106 (2014).

³² F. Andraschko and J. Sirker, Phys. Rev. B **89**, 125120 (2014).

³³ E. Canovi, P. Werner, and M. Eckstein, Phys. Rev. Lett. **113**, 265702 (2014).

³⁴ S. Sharma, U. Divakaran, A. Polkovnikov, and A. Dutta, Phys. Rev. B **93**, 144306 (2016); S. Bandyopadhyay, A. Polkovnikov, and A. Dutta, Phys. Rev. Lett. **126**, 200602 (2021).

³⁵ M. Sarkar and K. Sengupta, Phys. Rev. B **102**, 235154 (2020).

³⁶ S. E. Tapias Arze, P. W. Clayes, I. P. Castillo, and J.-S. Caux, SciPost Phys. Core **3**, 001 (2020).

³⁷ S. Aditya, S. Samanta, A. Sen, K. Sengupta, and D. Sen, Phys. Rev. B **105**, 104303 (2022).

³⁸ B. Mukherjee, S. Nandy, A. Sen, D. Sen, and K. Sengupta, Phys. Rev. B **101**, 245107 (2020).

³⁹ B. Mukherjee, A. Sen, D. Sen, and K. Sengupta, Phys. Rev. B **102**, 075123 (2020).

⁴⁰ B. Mukherjee, A. Sen, and K. Sengupta, arXiv:2112.14791.

⁴¹ A. Haldar, D. Sen, R. Moessner, and A. Das, Phys. Rev. X **11**, 021008 (2021).

⁴² M. Sarkar, R. Ghosh, A. Sen, and K. Sengupta, Phys. Rev. B **103**, 184309 (2021).

⁴³ M. Sarkar, R. Ghosh, A. Sen, and K. Sengupta, Phys. Rev. B **105**, 024301 (2022).

⁴⁴ S. Aubry and G. André, Ann. Israel Phys. Soc **3**, 18 (1980).

⁴⁵ J. B. Sokoloff, Phys. Rep. **126**, 189 (1985); J. M. Luck, J. Stat. Phys. **72**, 417 (1993), and Phys. Rev. B **39**, 5834 (1989); J. Bellissard, in *From Number Theory to Physics*, edited by M. Waldschmidt, P. Moussa, J. M. Luck, and C. Itzykson (Springer, Berlin, 1992).

⁴⁶ X. Li, X. Li, and S. Das Sarma, Phys. Rev. B **96**, 085119 (2017); X. Li and S. Das Sarma, Phys. Rev. B **101**, 064203 (2020).

⁴⁷ S. Roy, T. Mishra, B. Tanatar, and S. Basu, Phys. Rev. Lett. **126**, 106803 (2021); A. Padhan, M. K. Giri, S. Mondal, and T. Mishra, Phys. Rev. B **105**, L220201 (2022); S. Roy, S. Chattopadhyay, T. Mishra, and S. Basu, Phys. Rev. B **105**, 214203 (2022).

⁴⁸ S. Roy, I. M. Khaymovich, A. Das, and R. Moessner, SciPost Phys. **4**, 025 (2018).

⁴⁹ T. Shimasaki, M. Prichard, H. E. Kondakci, J. Pagett, Y. Bai, P. Dotti, A. Cao, T.-C. Lu, T. Grover, and D. M. Weld, arXiv:2203.09442v2.

⁵⁰ A. Soori and D. Sen, Phys. Rev. B **82**, 115432 (2010).